Draft version March 5, 2024
Preprint typeset using LaTeX style emulateapj v. 5/2/11



# MEASURING THE GALACTIC DISTRIBUTION OF TRANSITING PLANETS WITH *WFIRST*

Benjamin T. Montet[1,4], Jennifer C. Yee[2,4], Matthew T. Penny[3,4]

(Dated: March 5, 2024)
*Draft version March 5, 2024*

## ABSTRACT

The *WFIRST* microlensing mission will measure precise light curves and relative parallaxes for millions of stars, giving it the potential to characterize short-period transiting planets all along the line of sight and into the galactic bulge. These light curves will enable the detection of more than 100,000 transiting planets whose host stars have measured distances. Although most of these planets cannot be followed up, several thousand hot Jupiters can be confirmed directly by detection of their secondary eclipses in the *WFIRST* data. Additionally, some systems of small planets may be confirmed by detecting transit timing variations over the duration of the *WFIRST* microlensing survey. Finally, many more planets may be validated by ruling out potential false positives. The combination of *WFIRST* transits and microlensing will provide a complete picture of planetary system architectures, from the very shortest periods to unbound planets, as a function of galactocentric distance.

*Subject headings:* Galaxy: structure — planets and satellites: detection — telescopes

## 1. INTRODUCTION

The *WFIRST* microlensing survey is designed to detect planets with masses as small as Mars both bound at separations of several au and free-floating (Spergel et al. 2015). In the course of that 5-year survey, it will give precise photometry of 56 million stars down to $H_{\rm AB} = 21.6$ during six 72-day campaigns. Bennett & Rhie (2002) have suggested that such a microlensing survey has the potential to detect tens of thousands of transiting giant planets. McDonald et al. (2014) explore the capability of a hypothetical *Euclid* microlensing survey to detect and characterize transiting planets. In this paper, we expand on the idea of Tanner & Bennett in Spergel et al. (2015) and consider in detail the ability of *WFIRST* to detect transiting planets and to confirm them directly from the *WFIRST* microlensing data. Because the majority of bright stars will have relative parallaxes measured from the *WFIRST* data (Gould et al. 2015), this microlensing survey has powerful implications for the discovery of both transiting and microlensing planets at a wide range of galactic distances (McDonald et al. 2014).

To date, all detected planetary systems not found by microlensing have been found in the local neighborhood, in large part due to the difficulty of detecting planets farther away. Most techniques for detecting planetary systems rely on detecting light from the host star, which biases them to detections of relatively nearby planetary systems. For example, radial velocity surveys (e.g. Udry et al. 2007; Ford 2014), primarily targeted bright, nearby ($\lesssim 100$ pc) FGK stars (Valenti & Fischer 2005; Ammons et al. 2006).

The *Kepler* mission (Borucki et al. 2010) had the most power to detect transiting planets farther away, with discoveries out to a kiloparsec (Lillo-Box et al. 2014; Barclay et al. 2015; Quinn et al. 2015). Even in this limited volume, the mission has found some surprising differences between the local neighborhood and more distant regions of the galaxy. In particular, the number of hot Jupiter systems discovered by *Kepler* suggests an occurrence rate approximately 50% of that suggested by RV detections of hot Jupiters in the solar neighborhood. RV surveys estimate an occurrence rate for hot Jupiters on the order of 1% (Cumming et al. 2008; Mayor et al. 2011), while data from the *Kepler* mission suggest an occurrence rate of $0.4\% \pm 0.1\%$ (Howard et al. 2012). While the difference between the two fields is known, the explanation is unclear. Studies have invoked stellar metallicity (Howard et al. 2012; Wright et al. 2012; Dawson & Murray-Clay 2013), stellar age (Schlaufman & Winn 2013), and stellar multiplicity (Wang et al. 2014, 2015a). Regardless, this result suggests that planet occurrence rate may be affected by the local galactic environment.

The *K2* mission is providing the first opportunity to understand the differences in planet populations across the galaxy. After the failure of its second reaction wheel, *Kepler* became *K2* and switched to an observing mode in which it is observing a series of fields in the ecliptic plane for $\sim 70$ days at a time. This new mission has led to catalogs of transiting planet candidates (Foreman-Mackey et al. 2015; Vanderburg et al. 2016) as well as statistically validated planets (Montet et al. 2015; Crossfield et al. 2016). By the end of the *K2* mission, it will observe $\sim 20$ fields, providing an opportunity to probe variations in planet occurrence along different lines of sight through the galaxy. Nevertheless, because *K2* is still limited to observations of bright stars, it will only probe planets within $\sim 1$ kpc of the Sun.

Previously, OGLE-III (Udalski et al. 2002a,b) conducted searches for transiting planets in microlensing data, leading to several detections (e.g. Dreizler et al. 2003; Konacki et al. 2003; Bouchy et al. 2005). However, these detections have been limited to a small number of giant planet candidates. The SWEEPS survey also searched for transiting planets towards the bulge, finding

bmontet@uchicago.edu
[1] Department of Astronomy and Astrophysics, University of Chicago, 5640 S. Ellis Ave., Chicago, IL 60637, USA
[2] Smithsonian Astrophysical Observatory, 60 Garden Street, Cambridge, MA 02138, USA
[3] Department of Astronomy, Ohio State University, 140 West 18th Avenue, Columbus, OH 43210, USA
[4] Sagan Fellow

14 additional giant planet candidates (Sahu et al. 2006; Clarkson et al. 2008). Microlensing is often considered the only technique that offers the opportunity to probe large numbers of planets as far away as the galactic bulge (Batista et al. 2014; Calchi Novati et al. 2015). However, as we will show, the *WFIRST* microlensing data will enable the detection of potentially tens of thousands of short-period planets at comparable distances via the transit method. This gives it the opportunity to make a detailed measurement of the occurrence rate of short-period planets at a range of galactic distances. Among other things, this could address the discrepancy between the occurrence rate of hot Jupiters in the *Kepler* field and the solar neighborhood, and if the galactic bulge has a lower bulk planet occurrence rate than the local neighborhood (Penny et al. 2016a). Furthermore, as discussed in McDonald et al. (2014), a microlensing survey that detects transiting planets has different selection biases than the *Kepler* and *K2* surveys, which selected a fraction of the stars in the field for which to download postage stamps before observing each field.

The potential of *WFIRST* to detect large numbers of transiting planets is complicated by the difficulty of directly confirming those planets by traditional methods. In general, because the host stars of *WFIRST*-detected transiting planets will be so faint, it will not be possible to conduct followup RV observations to confirm their masses and rule out false positives. However, building on the experience from *Kepler* (Morton & Swift 2014), we will show that there are several measurements based on the *WFIRST* data alone that can be used to directly confirm or validate these transiting planets.

In this paper, we consider the capability of the upcoming *WFIRST* mission to detect, confirm, and characterize transiting planets and the distribution of those planets in the galaxy. In Section 2, we compare the *WFIRST* photometry to that of *Kepler* and describe the properties of our injected, detectable planets. In Section 3, we study the sensitivity of *WFIRST* to detecting transit events and project the possible yield for the mission. In Section 4, we discuss potential strategies to directly confirm individual transiting planets discovered by *WFIRST*. In Section 5, we discuss how systems can be statistically validated by searching for signatures of false positive events in the data. In Section 6, we discuss the galactic distribution of planets uncovered by *WFIRST*. We conclude in Section 7.

## 2. SIMULATING *WFIRST* TRANSIT DETECTIONS

### 2.1. *Assumed Parameters of the* WFIRST *Microlensing Survey*

#### 2.1.1. *Survey Duration and Cadence*

Based on the description in Spergel et al. (2015), *WFIRST* will cycle between ten pointings to tile 2.8 square degrees of the sky towards the galactic bulge. At each pointing, the telescope will observe for 52 seconds, returning to the same pointing every 15 minutes. The microlensing campaign will encompass six 72-day campaigns spread over five years. In this paper, we assume that the observations will be staggered, with three campaigns each separated by six months at the start of the mission and three additional campaigns each separated by six months at the end of the mission. The exact timing of the campaigns is inconsequential for the search for transiting planets, and only slightly affects the search for transit timing variations in the data. We assume that all data will be taken in the W149 band (0.927–2.000$\mu$m) with the exception of one data point every 12 hours in the Z087 filter (0.760–0.977$\mu$m), i.e. one Z087 data point for every 47 obtained in W149. The true *WFIRST* bandpass, W149, is a broadband filter spanning most of the near-IR (0.93-2.00 $\mu m$). In calculating the observed flux for our target stars we assume W149 $= (J + H + K)/3$; in assuming limb darkening models for each star we take $H$ band as a proxy for W149.

#### 2.1.2. *Photometric Noise*

We consider photometric noise following the standard CCD signal-to-noise equation. We use the values from the science definition team (SDT) report (Spergel et al. 2015) for the photometric zeropoint of the detector, as well as the bias, read noise, gain, dark current, and sky brightness. This report assumes (perhaps conservatively) an error floor in the photometry of 1 mmag, which we add in quadrature to the calculations from the SDT. The SDT estimates of the noise are presented in AB magnitudes.

We compare the estimated noise to that of Gould et al. (2015), who find that, for saturated stars, the precision in a single observation in the W149 bandpass will scale such that

$$\sigma = 1.0 \times 10^{(2/15)H_{\rm Vega}-2} \text{ mmag}, \quad (1)$$

where $H_{\rm Vega}$ is the apparent $H$-band magnitude relative to Vega. For reference, $H_{\rm AB} - H_{\rm Vega} = 1.39$ mag.

Near the saturation limit of 16.1 mag, the SDT estimate of the precision is very similar to that of Gould et al. (2015). For significantly brighter stars, the Gould et al. (2015) estimate of the noise is markedly lower than the (Spergel et al. 2015) prescription. As saturated stars make up only a small fraction of the stars in the *WFIRST* field of view, the choice of noise model does not appreciably affect our results. For consistency, we only consider the Spergel et al. (2015) estimate of the noise throughout this analysis, noting that if the Gould et al. (2015) noise estimate is realized, the performance of *WFIRST* will be improved at the extreme bright end.

We compare both of these relations to the photometric precision of *Kepler* in Figure 1. To perform a direct comparison to *Kepler*, we make two corrections. First, we follow the *Kepler* convention of considering the average noise of observations binned over six hours, the "combined differential photometric precision" or CDPP (Christiansen et al. 2012). Second, the *WFIRST* bandpass is significantly redder than the *Kepler* bandpass. As transit searches focus on FGKM stars, with red colors, these stars appear brighter on the *WFIRST* detector than they would on the *Kepler* detector. To provide a fair comparison, for the *Kepler* stars, we use the $H$-band magnitude of the stars in the *Kepler* field.

The expectation is that *WFIRST* will achieve a relative precision of 1 part per thousand (ppt) in a single observation of a 15th magnitude star in the W149 bandpass (0.93-2.00 $\mu m$). This is equivalent to 200 parts per million (ppm) when binned over six hours, comparable to the precision of *Kepler* on a star with $r \approx K_p = 15$. However, since a typical G dwarf has an $R - H$ color

of 1.1, the same Sun-like star observed with *Kepler* and *WFIRST* would be observed at a higher precision with *WFIRST*, even after accounting for the typical extinction level of $A_H \approx 0.7$ mag toward the bulge.

In this work, we assume the photometric noise is white, so that there are no correlations between observations. Correlated noise can be the result of spacecraft systematics or stellar p-modes (Gilliland et al. 2010; Campante et al. 2011). The timescale for p-modes is inversely proportional with stellar density: for G dwarfs, the granulation timescale is approximately five minutes; for M dwarfs, 30 seconds. Like *Kepler* data, for most stars observations will be spaced widely enough to capture a random phase of p-mode oscillations during each observation. As *WFIRST* has significantly larger levels of photon noise, the correlated stellar signals will be small by comparison, causing the while instrumental noise to dominate over any red astrophysical effects. Moreover, as *WFIRST* observes at much redder wavelengths, the complicating effects of stellar spots will be diminished.

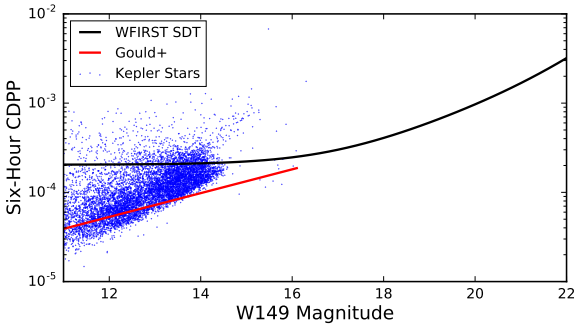


FIG. 1.— Expected noise properties of *WFIRST* in the W149 bandpass as a function of stellar magnitude. The black curve represents the estimates of the noise properties from the *WFIRST* SDT report. The red curve represents the estimates of the noise properties from Gould et al. (2015), who focus on saturated stars to detect asteroseismic modes using *WFIRST* data. In blue are actual observations of stars from *Kepler* for comparison. In all cases, we report the six-hour CDPP, or the noise averaged over six hours of observations.

### 2.2. *Simulated Light Curves*

We simulate individual transits by injecting a planetary signal into simulated *WFIRST* data using the prescription for the photometric noise described in the previous section. Every fifteen minutes, starting at a random phase, we collect an observation of the flux from this system: every twelve hours one observation is taken in Z087, while all other observations are in W149. We model the transit light curve with the transit model of Mandel & Agol (2002). We calculate limb darkening coefficients in each bandpass using the online tool developed and described in Eastman et al. (2013), which interpolates the Claret & Bloemen (2011) quadratic limb darkening tables.

Note that unlike the *Kepler* mission, each data point will consist of a single 52-second observation (290 s at Z087), rather than a series of binned observations over 30 minutes. Each observation will then sample one specific point on the transit light curve as opposed to an integrated measure of the observed flux, meaning morphological light curve distortions due to finite integration time will be minor in the *WFIRST* data (Kipping 2010).

### 2.3. *Simulated Host Star Population*

To simulate a realistic estimate of the stellar population in the *WFIRST* microlensing field, we develop a galactic population generated from the online Besançon models of the galaxy (Robin et al. 2003). To convert the returned apparent magnitudes to near-infrared simulated photometry, we apply the transformations of Bilir et al. (2008). We then apply a correction for interstellar extinction assuming the Cardelli et al. (1989) extinction law with $R_v = 2.5$, following Nataf et al. (2013). From the derived JHK magnitudes, we approximate the W149 magnitude for each star by assuming W149 = (J+H+K)/3.

We then apply a series of corrections to turn the Beasançon models into a realistic simulation of the stars observed by *WFIRST*. The Beasançon model outputs the properties and numbers of stars along a given sightline within a certain solid angle. Because each simulated field is not a perfect match to the *WFIRST* field, we weight each simulated star by the fraction of the simulated field that falls in the *WFIRST* field. We then apply a correction for the mass function in the bulge. The model assumes stars in the bulge follow the Salpeter IMF (Salpeter 1955). We downweight stars of mass $M < 0.5$ $M_\odot$ by a factor of $0.5/M$, which approximates the IMF of Kroupa (2001). We then apply a uniform correction to all stars to match the overall number of bulge main sequence stars near the *WFIRST* fields as measured by Calamida et al. (2015). Further details can be found in Penny et al. (2016b).

### 2.4. *Simulated Planet Population*

We simulate two planet populations. First, we simulate planets assuming the occurrence rate is the same as for the *Kepler* field. We assign planets around solar-type FGK stars following the planet occurrence estimates of Howard et al. (2012). We assign planet radii and orbital periods following the "Cutoff Power-Law Model" of Table 5 of that paper, and bulk occurrence rates for each spectral type following the authors' Table 4. For M dwarfs, we follow the relations of Morton & Swift (2014), specifically their "logflat+exponential" model of the period distribution from their Figure 7 and the radius distribution from their Figure 6. This leads to considerably smaller numbers of giant planets injected around M dwarfs than more massive stars, in line with observations from *Kepler*.

We also simulate planets taking host star metallicity into account. *WFIRST* will observe stars at large distances along the galactic metallicity gradient (Rolleston et al. 2000; Pedicelli et al. 2009). Observations suggest the average stellar metallicity changes by -0.05 dex/kpc along a line of sight moving radially outward from the center of the galaxy. Thus *WFIRST* is expected to observe stars at preferentially higher metallicities than the solar neighborhood. Indeed, simulations of the *WFIRST* field suggest the median G2V dwarf observable by *WFIRST* with W149 $< 19.5$ has [Fe/H] $= 0.26$ (Section 3.2). This is significant because radial velocity surveys have unveiled a correlation between giant planet occurrence and stellar metallicity (Fischer &

Valenti 2005; Johnson et al. 2010). Note, however, that the presence of small transiting planets does not appear to be affected by the host star's metallicity (Buchhave & Latham 2015).

To account for this metallicity effect, we weight the planets based on their radii and host star metallicity. Following Johnson et al. (2010), who find planet occurrence scales as $10^{1.2[\mathrm{Fe/H}]}$, we modify the likelihood of all planets with radii larger than 5 $R_\oplus$ by this factor. For the median star ([Fe/H] = 0.25), this factor increases giant planet occurrence by a factor of two.

## 3. TRANSITING PLANET DETECTION WITH *WFIRST*

### 3.1. *Detection of Transit Events*

After all transits have been simulated, we phase-fold on the known period and measure the significance of the observed transit depth. We use the same $7.1\sigma$ threshold as that used by *Kepler* to decide whether or not a transit is detected. We also require at least two transits during at least one season to be detected.

The $7.1\sigma$ threshold is not strictly appropriate for these simulations. It was chosen for *Kepler* so that there would not be more than one false positive with three "transits" out of 100,000 stars. *WFIRST* will observe a thousand times more stars, which would increase the threshold for detection. At the same time, we have required 2 transits to be detected in a single season. Since *WFIRST* will have six microlensing seasons, this means there will be $\sim 12$ transits over the course of the mission. Therefore, the effective detection threshold over the mission is higher than $7.1\sigma$. Finally, $7.1\sigma$ was chosen in the absence of correlated noise and systematics, so in practice the true threshold for planet detection in *Kepler* is higher because of the presence of these effects. Thus, we conclude that $7.1\sigma$ is a reasonable benchmark for the detection of planets, but the true threshold will have to be evaluated once the properties of the data are better understood.

Figure 2 shows an example light curve for a Jupiter-sized planet on a 3.0 day orbit around a W149 = 15.0 mag host star with impact parameter $b = 0.5$. The transit duration is approximately two hours. These transits can be seen by eye, even in the case of single transit events. Over the course of the mission, more than 150 transits of such a hot Jupiter would be observed, leading to approximately 1200 observations during the transit in the W149 bandpass. Moreover, approximately two dozen observations during the transit will be collected in the Z087 bandpass, which might be useful for confirmation of the planetary nature of this signal (Section 4). By fitting transit models and evaluating their likelihood, we measure a transit depth of $0.998 \pm 0.002\ R_J$, assuming perfect knowledge of the stellar host. This planet is detected at $\sim 500\sigma$.

Using our simulated light curves we calculate *WFIRST*'s sensitivity to planets as a function of radius and period. We simulate planets with radius and orbital period drawn from log-flat distributions over the ranges $[1, 16]\ R_\oplus$ and $[1, 72]$ days, respectively. We then assign an impact parameter for each simulated transiting planet drawn from a uniform distribution over the range $[0, 1]$. We assume the host star is a G-dwarf with radius $1R_\odot$. We then check to see which planets meet our detection threshold. The results are shown in Figure 3. We have chosen to present this calculation in terms of physical parameters rather than transit depth because they are more intuitive. However, since the radius of the host star is fixed, it is trivial to convert to transit depth if desired.

We find that, for the brightest stars observed by *WFIRST*, Neptune-sized planets with orbital periods shorter than one month will be easily detected in a single season of data. The mission will also recover many mini-Neptunes with periods shorter than 20 days, and is likely to recover a small number of planets smaller than 2 $R_\oplus$ with periods shorter than two days. Over the entire mission, *WFIRST* will be sensitive to a few Earth-sized planets with orbital periods shorter than two days orbiting the brightest stars. Of the 12 million stars with W149 < 19.5, the prospects for detecting super-Earths or mini-Neptunes are much lower, but the mission will detect the majority of Neptune-sized planets with periods less than a month and all transiting Jupiter-sized planets in that period range as well. We discuss expected planet yields in Section 3.2.

### 3.2. *Expected Planet Yield*

We use the simulations described in Section 2 to calculate the number of transiting planets that will be detected by *WFIRST*. We inject planets around the main-sequence dwarf stars brighter than W149 = 21.0. We use the same detection criteria as in Section 3.1, and thus, we limit the range of orbital periods to $P < 72$ days.

The results are shown in the left-hand panels of Figure 4. Assuming a *Kepler*-like planet population, we expect *WFIRST* to detect approximately 13,000 transiting planets orbiting dwarf stars with W149 < 19.5, the majority being giant planets orbiting F and G stars. Similarly, we expect *WFIRST* to detect 70,000 transiting planets orbiting stars with W149 < 21.0. The mission will also detect approximately 800 planets smaller than Neptune, the majority of which will be orbiting M dwarfs. While large, these numbers are not unexpected given that *WFIRST* will observe two orders of magnitude more stars than *Kepler*, which detected several thousand transiting planets.

The numbers are even more striking when taking into account the expected metallicity dependence on the occurrence rates of transiting planets (right-hand panels of Figure 3.2). In this case, we detect more than 150,000 transiting planets over the six seasons of the *WFIRST* mission. As expected, the number of small planets is unchanged, with the gains made entirely in the population of planets larger than Neptune. *WFIRST*, by completing this survey, will provide the best assessment of the effects of high metallicity on the population of giant planets, providing clues to the formation and evolution of these systems. With the development of multi-object NIR spectrographs for large telescopes like the VLT, reconnaissance spectroscopy for large numbers of faint stars to measure metallicities will be possible (Cirasuolo et al. 2012). We show the distribution of these planets with respect to the apparent magnitudes of their host stars in the *WFIRST* bandpass in Figure 5.

### 3.3. *Other Transiting Planet Detections*

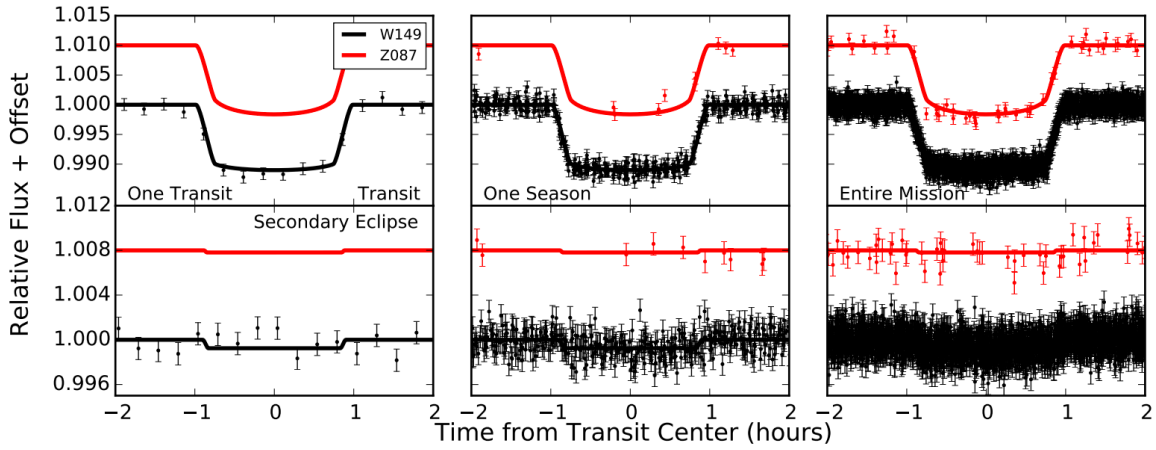


FIG. 2.— (top) Simulated transit photometry for a hot Jupiter on a three-day orbit around a Sun-like star with W149 = 15. In black is photometry from the W149 bandpass; in red, the Z087 bandpass. The left panel corresponds to a single transit. The middle panel corresponds to transits folded together over a 72-day observing season, while the right panel corresponds to six such seasons over the course of the mission. The transit simulated in all panels are identical. (bottom) Simulated secondary eclipses for the same planet, assuming its planet has an equilibrium temperature of 900 K. The secondary eclipse is then as deep as the transit of a 3 $R_\oplus$ planet across the same star and is detected at high significance by the end of the mission.

#### 3.3.1. *Single Transit Events*

*WFIRST* will also be able to detect large numbers of single transit events. Planets with no more than one transit per season do not meet our detection criteria. Such planets may or may not have a transit in a subsequent season. If a second transit is observed, there will be some ambiguity in the period because the data are not continuous. However, it should be possible to rule out a substantial fraction of the aliases by considering the non-detections and by estimating the period from the transit ingress and egress following Yee & Gaudi (2008). Even for the cases for which only one transit is observed, it should still be possible to place constraints on the period using these methods, and where possible, prompt RV observations would be extremely beneficial (Yee & Gaudi 2008). A few dozen singly transiting were planets detected in the *Kepler* and *K2* data, largely through visual inspection (Wang et al. 2015b; Osborn et al. 2016; Uehara et al. 2016; Foreman-Mackey et al. 2016). The probability of detecting a singly transiting planet with *WFIRST* scales as $P^{-5/3}$, so most detections of single transits will be of planets with shorter orbital periods. However, given the large number of stars observed by *WFIRST*, there should still be large numbers of planets with periods of a few years. While the period distribution of expected microlensing planets with *WFIRST* peaks at periods of about ten years, there should be a large number of massive planets with periods 2-5 years detected as well. These longer-period planets offer the opportunity for direct comparison to the *WFIRST* microlensing planet population, which will have periods of a few years. They may also be compared to measurements of the occurrence rates of long-period planets from the combination of long-term RV accelerations with direct imaging surveys (Montet et al. 2014, Gonzales et al. in prep).

#### 3.3.2. *Planets Around Evolved Stars*

Finally, we note that our analysis is limited to dwarf stars towards the bulge brighter than W149 = 21.0. While planets have been detected around evolved stars in transit (Lillo-Box et al. 2014; Barclay et al. 2015; Quinn et al. 2015), and through radial velocities (Johnson et al. 2011; Otor et al. 2016), the occurrence rate of short-period planets around evolved stars are too poorly understood to enable a reliable estimate of their yield in *WFIRST*. However, given the photometric precision from Section 2.1.2 and scaling from Section 3.1, giant planets

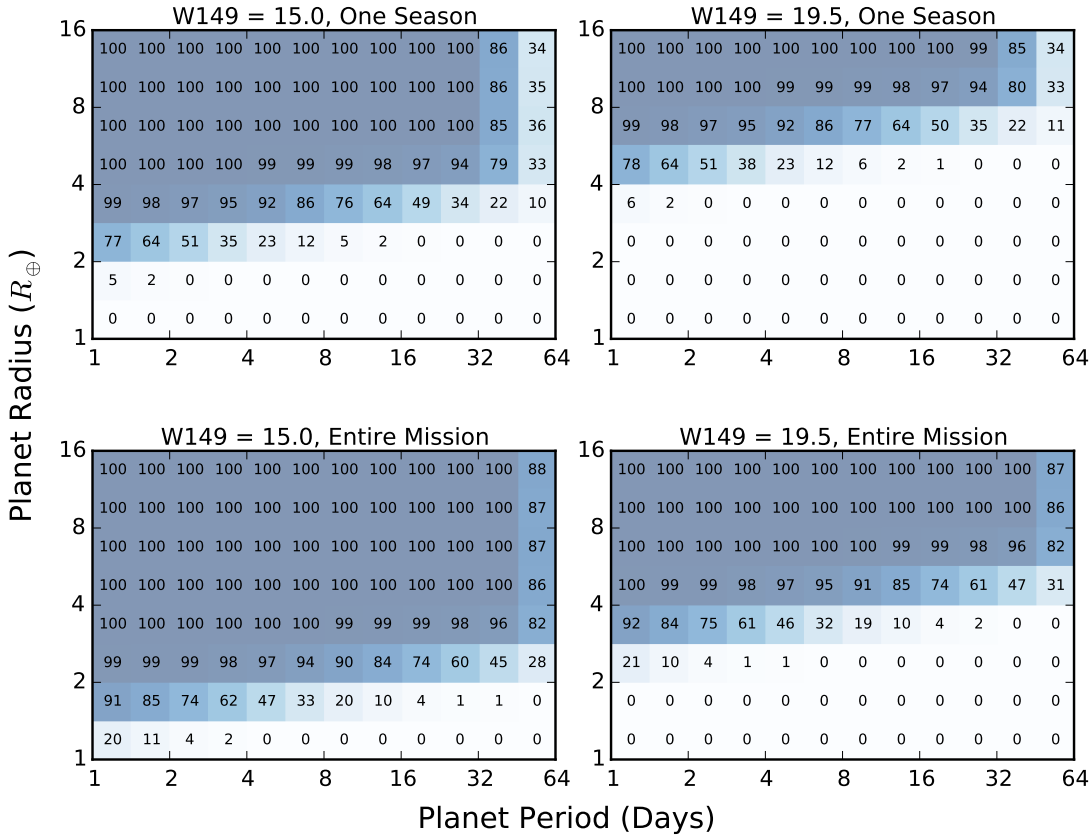


FIG. 3.— Detectability of planets transiting a Sun-like star in simulated *WFIRST* data by analyzing (top) one season of data and (bottom) data from the entire mission. Around very bright stars (W149 = 15.0) nearly all Neptune-sized planets and larger with orbital periods shorter than the seasonal baseline will be detected in a single season of data. To qualify as a detection, we require at least two transits in a single observing season, but not necessarily in all seasons.

will be detectable around evolved stars (i.e. given that $3R_\oplus$ planets are detectable around a $1R_\odot$ star, a $12R_\oplus$ planet should be detectable around a $4R_\odot$ star.). As *WFIRST* will observe large numbers of evolved stars towards the bulge, it will provide the best measurement to date of the occurrence rate of giant planets in short orbits around evolved stars.

## 4. CONFIRMATION AND CHARACTERIZATION OF TRANSITING PLANETARY SYSTEMS

The major challenge for transiting planet studies is to verify that the observed transiting object is a planet rather than a false positive. Multiple astrophysical events can be mistakenly identified as transiting planets. First, because of degeneracy pressure, Jupiters, brown dwarfs, and low-mass M stars all have similar radii (Chabrier & Baraffe 1997). Therefore, detection of a Jupiter-radius transit depth alone is insufficient to claim a planetary detection. Second, a false positive can occur in the case of blended light, when the star in question in the aperture is actually the combined light of multiple stars. For example, an unresolved, background eclipsing binary could be blended with the primary target star. Similarly, the primary itself could be an eclipsing binary blended with the chance alignment of a background star or the light of a hierarchical triple third star. While these degeneracies are easily resolved with RV observations, those will not be possible for most *WFIRST* transit candidates. However, previous studies have shown in the case of *Kepler* that it is possible to validate transiting planet candidates by ruling out various false positive scenarios (Morton 2012; Morton et al. 2016). Here we explore various means to confirm *WFIRST* transiting planet candidates. In Section 5 we consider ways to validate or rule out false positives for planets that cannot be confirmed directly. See also McDonald et al. (2014) for a discussion of these topics with respect to a *Euclid* microlensing survey.

### 4.1. *Multiple Planet Systems*

If *WFIRST* observes transits from multiple planets around a single star, this by itself significantly increases the probability that the transits are indeed due to real planets rather than astrophysical false positives. The initial *Kepler* data release contained 444 multiple-candidate

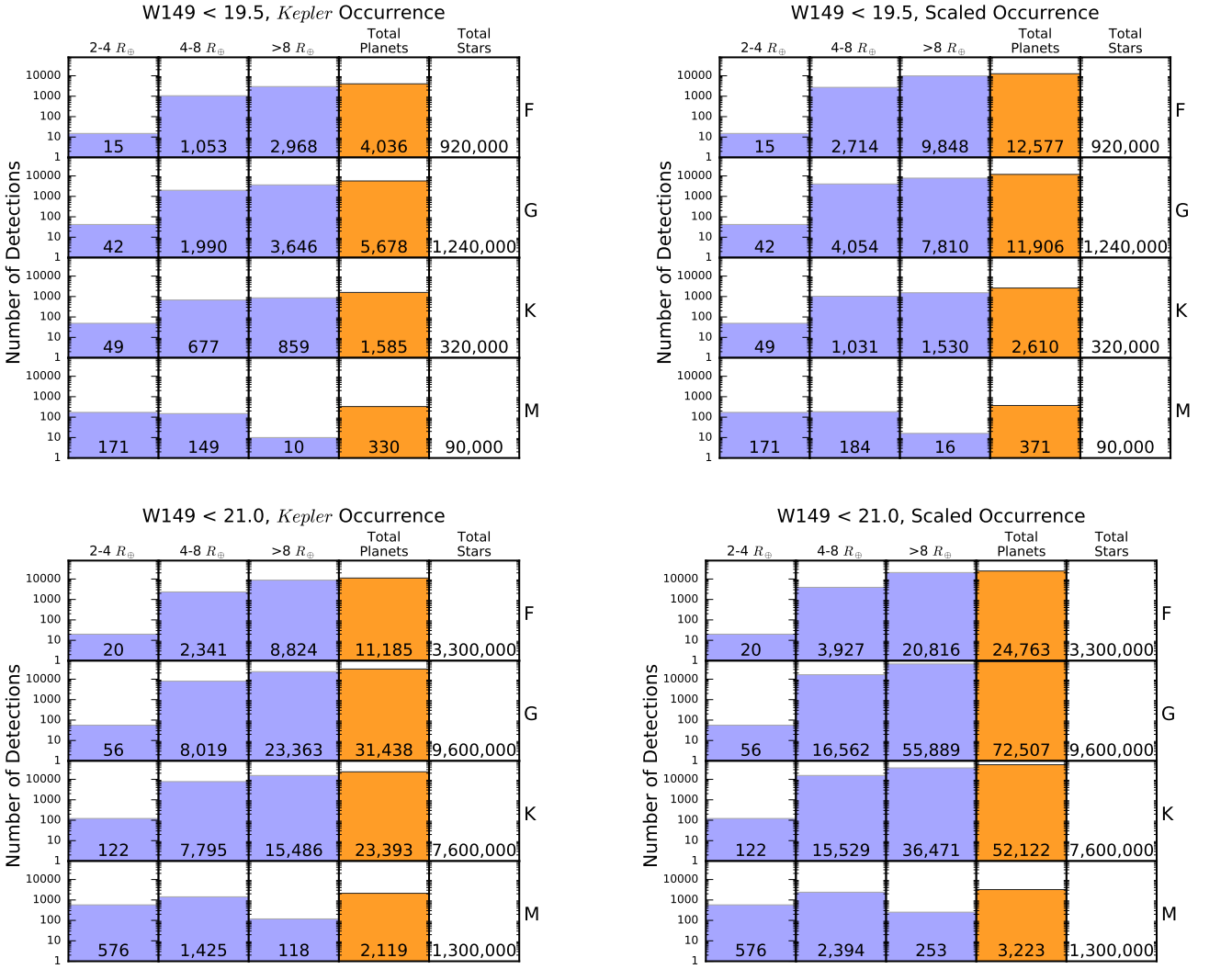


FIG. 4.— (Top) (Left) Expected yield of transiting planets orbiting dwarf stars brighter than W149 = 19.5 in the *WFIRST* data as a function of planet size and stellar type, assuming the planet occurrence is the same as that in the *Kepler* field. *WFIRST* will detect thousands of Jupiter sized planets, but also more than 100 planets smaller than Neptune, mainly around M dwarfs. (Right) The same, but assuming the occurrence rate of planets larger than 5 $R_\oplus$ follows the metallicity relation of Johnson et al. (2010). (Bottom) Same as the top, with a limiting magnitude of W149=21.0. In this case, more than 150,000 transiting planets could be detected by the end of the mission.

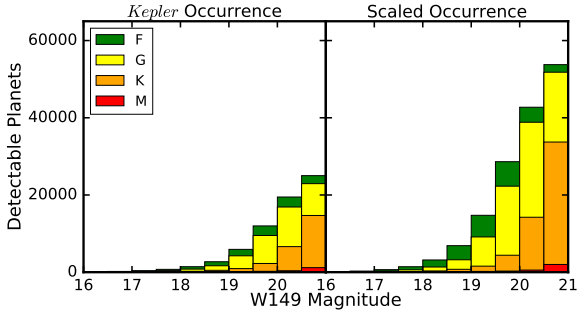


FIG. 5.— Distribution of apparent magnitudes of the host stars of planets detectable by *WFIRST*. Similar to the *Kepler* mission, the vast majority of planets will be found around relatively faint stars.

systems from a total of $\sim$ 1600 candidate systems (see Lissauer et al. 2011, 2012). Thirty-eight of those systems have $r > 3R_\oplus$ and $P < 72$ days, making them easily detectable by *WFIRST*. It would not be surprising for *WFIRST* to discover more than one thousand planetary systems with multiple transiting planets over the course of its mission.

### 4.2. *Transit Timing Variations*

If there are multiple planets in a system, this opens the possibility of measuring transit timing variations (TTVs). TTVs are the deviation of the time of the transit center from a linear ephemeris and are caused by dynamical interactions between the various bodies in the system (Holman & Murray 2005; Agol et al. 2005; Lithwick & Wu 2012). The exact nature of any TTV curve depends on the architecture of any particular TTV system: two planetary systems with identical planets but different orbital eccentricities, arguments of periapse, or longitudes of ascending node would exhibit different TTV signals. They are the most straightforward way for *WFIRST* to directly confirm the planetary nature of transit signals.

*Kepler* has had enormous success at measuring TTV signals. They have been used to confirm the planetary nature of transiting signals (Holman et al. 2010; Fabrycky et al. 2012; Ford et al. 2012; Xie 2013), to detect the presence of non-transiting planets (Ballard et al. 2011; Nesvorný et al. 2012, 2013), and to infer masses and eccentricities of planetary systems (Hadden & Lithwick 2014; Jontof-Hutter et al. 2015, 2016). Based on data from the *Kepler* mission, TTV signals have been analyzed around more than 2,500 KOIs (Holczer et al. 2015, 2016). They have detected 260 KOIs with TTVs on timescales $> 100$ days, i.e. likely to be due to a companion rather than an astrophysical false positive. Of these, 163 have TTV amplitudes larger than 15 minutes (see below). Based on the number of planets we expect *WFIRST* to be able to detect and the timing precision we expect the mission to achieve on individual transits 4.2, hundreds of systems with observable TTVs should be detected over the observing campaign.

We should note that *WFIRST* TTVs will have a few differences with respect to *Kepler* TTVs. The longer time baseline (5 years as opposed to 4) will enable the possible detection of transit timing signals with longer periods, such as those due to the Roemer delay from a hierarchical binary star or the orbital evolution of a giant planet in a short orbit (Ragozzine & Wolf 2009; Maciejewski et al. 2016). However, the large gaps between seasons result in degeneracies in the TTV solutions. At the same time, *WFIRST* TTVs will be less severely affected by starspots. Starspots complicate the measurement of TTVs by distorting the light curve both in and out of transit. Since *WFIRST* will observe in the near-IR, where the effects of starspots are significantly minimized due to their lower contrast, this reduces the possibility of significant starspot-induced timing errors.

To better understand the detection of TTVs with *WFIRST*, we simulate transit events in order to estimate the precision to which we will be able to measure transit times. We model our benchmark system after Kepler-9b and Kepler-9c, the first planets confirmed via TTVs (Holman et al. 2010). We use orbital periods for the two planets of 19.2 and 38.9 days. *Kepler* has shown that less massive planets more often exhibit TTVs than more massive planets (Mazeh et al. 2013), and yet a transit must be detected in order to measure a TTV. Thus, we simulate planets near the bottom of our detectability contours in order to understand a typical TTV signal seen by *WFIRST*. We assume the two planets are mini-Neptunes with masses of 10 $M_\oplus$ and radii of 3 $R_\oplus$. These are significantly smaller than the real Kepler-9 planets leading to smaller TTVs and larger uncertainty in the measured time of transit center. We simulate transits of these planets orbiting a Sun-like star with W149 = 15.0, so that the photometric precision on each data point is 1 part per thousand, assigning impact parameters at random.

First, we consider the precision with which *WFIRST* can measure the times of individual transits. We focus on the precision for the inner planet, because more transits will be observed over the course of the *WFIRST* mission. To begin, we fit a transit model to simulated transits for the inner planet, fixing the limb darkening to that predicted by Claret & Bloemen (2011) for a Sun-like star in the H-band but allowing the transit parameters to vary.

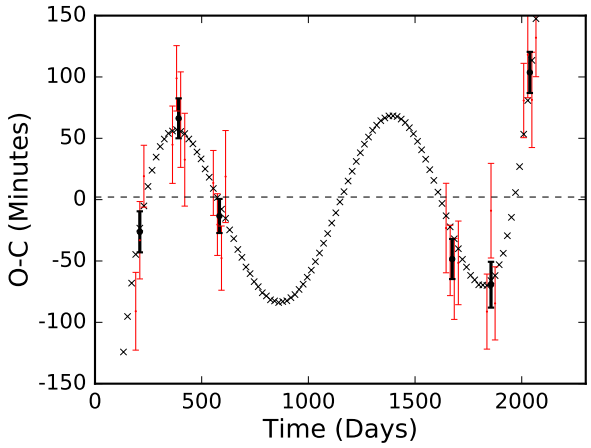


FIG. 6.— Simulated TTV signal from a two-planet system as observed by *WFIRST* (see Section 4.2). Gray X labels correspond to the actual deviation form a linear ephemeris for each individual transit. For those observed during a simulated *WFIRST* season, typical uncertainties are added to the observed time of transit with data shown in red. The black points correspond to binned observations over an entire season. This hypothetical system would be confirmed by TTV observations in *WFIRST* data.

After simulating many transits, we find a median uncertainty in the measured transit time for each individual transit of 28 minutes. Over the course of a single season, several transits will be observed. If we phase-fold over all observed transits inside an observing season, we find a median uncertainty in the average transit time of the folded transit of 15 minutes.

Given these expectations for the measurement precision, we then consider if *WFIRST* data can be used to identify interacting systems with TTVs. We use TTVFast (Deck et al. 2014) to integrate our test system as a dynamically interacting planetary system over a simulated *WFIRST* campaign. The simulated deviations of the transit times are shown as the gray X's in Figure 6. We then simulate observations of these systems over hypothetical *WFIRST* seasons. For each observed transit, we add a random offset drawn from a uniform distribution on the range [25 minutes, 40 minutes], similar to the predicted scatter on measurements of the times of individual transits, and assign an uncertainty on the observed time of transit equal to this value (red points in Figure 6). The average time of transit for each particular season is also shown (black points). We purposefully schedule the *WFIRST* seasons to coincide with the smallest observed TTV signal to simulate a worst-case scenario.

Fitting only the transit times of the inner planet, we find that a dynamically interacting planet model fit the data considerably better than a linear ephemeris ($\Delta\chi^2 = 64$). In this case, these planets would be easily confirmed via *WFIRST* observations. It is very difficult to contrive a set of observations of this planetary system that would not have detectable TTVs with *WFIRST*. However, the inferred masses of the transiting planets are a function of the unknown eccentricity: a pair of 10 $M_\oplus$ planets or a pair of 25 $M_\oplus$ planets can both explain the observed TTVs.

Given this simulation, we conclude that *WFIRST* TTVs can be used to confirm planets, but will not be robust for measuring their masses. However, for the

brightest stars, it may be possible to identify particular transits that would be useful for precise determination of planet masses. These transits could then be targeted for observations from other facilities in order to measure their TTVs. Furthermore, based on demographics alone, this method will be best for confirming smaller planets, which are more likely to have companions to produce a TTV signal. In contrast to small planets, most giant planets are most often detected in isolation, without an additional transiting companion (Steffen et al. 2012). However, the detection of TTVs requires the existence of a second planet. So far, there is only one hot Jupiter system with detected TTVs induced by the presence of an additional planet (Becker et al. 2015). We expect only a few of the hot Jupiters detected by *WFIRST* will be confirmed by this method.

### 4.3. *Secondary Eclipses*

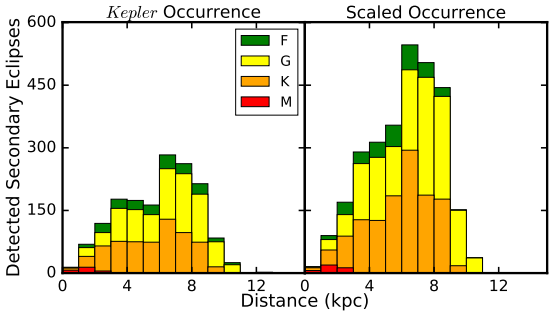


FIG. 7.— Simulated number of detected secondary eclipses of giant planets as a function of host star spectral type and distance. If planet occurrence is the same as the *Kepler* field, we expect *WFIRST* to directly detect secondary eclipses of 1,700 planets. Assuming a local scaling with stellar metallicity, *WFIRST* will detect secondary eclipses of 2,900 planets. In both cases, the detected secondaries will predominantly be those of hot Jupiters transiting G and K dwarfs.

Although *Kepler* shows that hot Jupiters are unlikely to exhibit TTVs, they can be confirmed by observations of their secondary eclipses. The depth of the secondary eclipse yields a measurement of the brightness temperature, and thus the flux in that bandpass (e.g. Charbonneau et al. 2005). Previous experience from *Kepler* shows that with *Kepler* data alone it is difficult to confirm planets via secondary eclipses. While *Kepler* detected thousands of planets, it was only able to confirm planetary systems via detection of their phase curves and secondary eclipses for a handful of these (e.g. Esteves et al. 2013; Quintana et al. 2013; Angerhausen et al. 2015). Because the *Kepler* bandpass spans approximately $0.4 - 0.9$ $\mu$m, near the peak of a typical stellar spectrum but far bluer than the typical planetary spectrum, only the hottest, largest planets are detectable by their own emission. However, *WFIRST*, with its primary bandpass spanning 0.927-2.000 $\mu$m, will be significantly more effective at observing planetary emission directly.

The bottom panels of Figure 2 show the secondary eclipses of a typical hot Jupiter, which has an eclipse depth equivalent to the transit of a $3R_\oplus$ planet. As a more extreme example, WASP-12 b's secondary eclipse depth integrated accros the *WFIRST* bandpass is nearly 2 parts per thousand (Croll et al. 2011; Stevenson et al. 2014a), matching the transit depth of a 4.9 $R_\oplus$ planet. Figure 3 shows that we expect detections of secondary eclipses of analogous planets to be detected around stars as faint as W149 = 21.0, by the end of the mission. Even smaller, cooler planets will be detected in secondary eclipse around the million stars with W149 brighter than 15.0.

To determine the feasibility of observing secondary eclipses with *WFIRST*, we model the secondary eclipses of each transiting planet injected in Section 3.2. We estimate the relative flux of each planet and its host star in the *WFIRST* bandpass assuming the planet radiates as a perfect blackbody. This decision is a simplification of the nonthermal physics of exoplanet atmospheres. By comparing to theoretical spectra from the BT-Settl spectral library of Baraffe et al. (2015) as well as actual near-IR observations of hot Jupiters, we find it is too optimistic in the observed planet flux by approximately a factor of two, so we divide all estimated fluxes by that factor to account for this approximation.

We assume circular orbits for all planets, so that the duration of the secondary eclipse is identical to the transit duration, and assume no limb darkening or spatial variations in the received flux from the planet itself. We attempt to detect each secondary eclipse in the same manner we detect each transit, declaring the eclipse detected if it is observed at $7.1\sigma$, but making no *apriori* assumptions about the time of secondary in our search.

By the end of the mission, of the planets detected in our simulations in Section 3.2, we expect to detect approximately 1,600 planets in secondary eclipse if the planet occurrence rate is the same as the *Kepler* field, and 2,900 planets if the planet occurrence rate scales with metallicity in the same way as it does in the solar neighborhood. As shown in Figure 7, these eclipses are predominantly around G and K stars at a few kpc. F stars are too luminous relative to the planets for the secondary eclipses to be regularly detected, while giant planets are too rare around M dwarfs to detect their secondaries in significant numbers. *WFIRST* will detect more secondary eclipses than have been detected for all known exoplanets to date. For many of these systems, *WFIRST* could plausibly detect phase curves as well, as we discuss in Section 5.3.1.

If secondary eclipses are to be used to confirm planetary systems, observers will need to be able to separate true secondary eclipses from false positive events. It is unlikely that a background binary would be observed with a period as close to that of a transiting system to mimic a secondary eclipse signal, especially with a five-year time baseline. The only conceivable false positive scenarios involve a single eclipsing binary system masquerading as a transit and secondary eclipse. As a planetary secondary eclipse depth will represent the eclipse of a $\sim 1000$ K body, most stellar-stellar secondary eclipses will be too deep to mimic a stellar-planetary secondary eclipse. The most plausible false positive case is then a significantly blended stellar binary, blended either because of a bright background star, or because the binary itself is in the background of the target star.

As we discuss in Section 5.1, because of the small pixel scale for *WFIRST* the rates of both of these events should be fairly low, similar to *Kepler* (Morton & Johnson 2011). Even better, in many cases stellar-stellar secondary eclipses should be discernible from stellar-

planetary eclipses as the durations of ingress and egress should be much longer for stellar-sized objects than for planetary-sized objects. Additionally, high-resolution reconnaissance spectroscopy of these systems should enable us to detect spectral signatures of blended stars in each system if they exist. Therefore, the vast majority of candidate planetary secondary eclipse detections should be real events, with a relatively small minority being astrophysical false positives.

## 5. VALIDATION OF TRANSITING PLANETARY SYSTEMS

If a planet cannot be directly confirmed, it is often still possible to statistically validate the transit signal as caused by a planet at a high degree of confidence. Morton (2012) developed a method to validate systems efficiently which has been used to validate more than 1,200 planets in the original *Kepler* field. Morton (2015) generalize this method to any field, which has enabled the first catalogs of validated transiting planets with data from the *K2* mission (Montet et al. 2015). If the potential transit signal is actually caused by a brown dwarf or binary star system, there are several options for identifying this.

### 5.1. *Blended Light*

Blended light from multiple stars in the PSF or in a given pixel crates two problems for reliably detecting transiting planets. First, the extra light can dilute a real planetary transit causing it to appear shallower than otherwise expected. Dilution could then lower the SNR of observed transit signals, complicating the detection of small planets orbiting faint stars. Second, the dilution can be so severe that a background eclipsing binary mimics a transiting planet signal.

The *Kepler* mission had smaller pixels on the detector relative to wide-field, ground-based transit searches, making the stellar density per pixel lower (Morton & Johnson 2011). As a consequence, it had a significantly lower rate of false positive transit signals than previous transit search missions from the ground.

The Kepler Input Catalog contains approximately 4.5 million stars brigher than $K_p = 21$ that were observable by the detector's 94.6 million pixel detector (Haas et al. 2010), meaning on average there were 4.8 stars for every 100 pixels. *WFIRST* has much smaller pixels than *Kepler* (0.11" vs. 4"), but the campaign fields are significantly more crowded, containing approximately 300 million stars brighter than W149 = 28 (see Figure 6 of Gould et al. 2015, for an estimate of the stellar density as a function of magnitude). As a result, the field will contain approximately 10 stars per 100 pixels within this limit, for a crowding rate approximately a factor of two larger than *Kepler*. The *Kepler* limit is five magnitudes fainter than the limit for the faintest stars in the exoplanet survey ($K_p = 16$), where here the *WFIRST* limit is seven magnitudes fainter than the faintest planet hosts considered. Many of these potential blended stars will immediately be able to be ruled out as causes of false positive events, if their contribution to the light curve is less than the observed transit depth. The same techniques used to identify blends for *Kepler* and ground-based transit surveys should continue to be relevant for *WFIRST*. In particular, observations of centroid shifts of the photocenter of light during transit events and differences in the depth of alternating transits should provide information about false positives.

### 5.2. *Z087 Photometry*

Transits of a dark object across the face of a star should be, to first order, achromatic. False positive events caused by eclipsing binaries, where multiple objects are self-luminous, will have wavelength-dependent depth variations as different portions of the stellar SEDs are sampled at different bandpasses. Multiband photometry can then be used to separate transiting planets from background eclipsing binary events.

In the *WFIRST* mission, one data point will be collected every 12 hours in the Z087 filter, or one data point for every 47 obtained in W149. For the example hot Jupiter transiting a Sun-like star with a three-day period, only 24 data points will be obtained during the transit event in Z087 over the entire mission, approximately one data point for every six transits. The situation will be even worse for planets with longer orbital periods, or those with higher impact parameters and shorter transit durations.

We can assume that the transit ephemeris and orbital parameters are known from the W149 photometry used to detect planetary transit signals. Therefore, we only need to fit three parameters in the Z087 transit model: two to describe the limb darkening and one to describe the transit depth. For this case, fitting the Z087 photometry we measure a transit depth to a precision of 3.7%. Therefore, an 11% difference in transit depth between Z087 and W149 is the minimum detectable difference at $3\sigma$ confidence using data from the entire mission. This is sufficient to rule out many, but not all, stellar false positives.

For example, a false positive M7 dwarf with a temperature of 2900 K and a radius equal to Jupiter's has a flux density smaller than the Sun by a factor of 5.7 in the W149 filter and 11.6 in the Z087 filter, leading to a 9% change in the observed transit depth between the two filters. A moderate increase in the cadence of Z087 observations would be required in order to detect these depth variations to identify false positives. However, as long as the orbit is aligned such that secondary eclipses are observable from Earth, this star would induce a 2 ppt secondary eclipse, easily detectable with *WFIRST* photometry.

While Z087 photometry may be useful at the current cadence in extreme cases, secondary eclipse photometry will be much more significant, as long as the companion's orbit is aligned such that secondary eclipses are visible. An increased rate of *Z*087-band photometry, perhaps as often as once every three hours, would provide more opportunities to separate transiting hot Jupiters from self-luminous brown dwarfs or giant planets.

Finally, we note that validation via wavelength dependent transit depth can be complicated by the effects of starspots. This is true both in the case where the planet crosses starspots, affecting the light curve shape, and where starspots are located at different latitudes, affecting the transit depth and out-of-transit flux. Due to the nature of the W149 bandpass, we expect spots to have a minimal effect on the observed light curve. They will be more prevalent in the Z087 photometry, but still diminished relative to the *Kepler* bandpass.

### 5.3. *Phase Curves*

Although a transit is the most obvious signal in a light curve of a planet orbiting a star, the companion planet affects the observed light curve throughout its orbit. Phase curve variations are the sum of three separate effects: thermal emission, reflected light from the host star, relativistic Doppler beaming, and ellipsoidal variations. These variations have been discussed in previous work as a method to measure planetary masses (Faigler & Mazeh 2011; Shporer et al. 2011; Mislis et al. 2012), to detect new transiting objects (Faigler et al. 2015), and to understand the atmospheres of transiting planets (Knutson et al. 2007; Faigler & Mazeh 2015).

#### 5.3.1. *Thermal Emission*

A detection of a secondary eclipse is the detection of a planetary atmosphere. At the moment before secondary eclipse ingress, the observed flux is the combined flux from the star and the day side of the planet, while observations during the secondary eclipse represent light from the star alone. If the planet has a large flux differential between its day side and night side, then we might expect to see quasi-sinusoidal variations in the light curve over the course of each orbit as the phase of the planet varies. Phase curves have been observed for nearby transiting giant planets (Knutson et al. 2007). These enable a direct characterization of day-night temperature contrasts, rapid winds in the atmospheres of these planets, and hot-spot offsets away from the substellar point of tidally locked systems (e.g. Knutson et al. 2007, 2009; Stevenson et al. 2014b).

Here, we use WASP-43 b Hellier et al. (2011) as a test case to explore the detectability of thermal emission of hot Juptiers with *WFIRST*. *HST* and *Spitzer* phase curves of WASP-43 show the planet has a dayside temperature of 1700 K but a nightside temperature of 500 K (Stevenson et al. 2016). They also show that the peak in observed emission from WASP-43 b occurs $40 \pm 3$ minutes before the secondary eclipse, or $12.3 \pm 1.0$ degrees east of the planet's substellar point. We analyze simulated *WFIRST* data to see if these signals would be detectable.

The day-night difference leads to an observable phase curve primarily in the mid-infrared, at longer wavelengths than the *WFIRST* bandpass. From the emission spectrum of WASP-43b of Stevenson et al. (2016), the observed peak-to-peak amplitude of the phase curve in the 4.5 $\mu$m *Spitzer* bandpass is $3.99 \pm 0.14$ parts per thousand; the expected signal integrated across the *WFIRST* bandpass is 0.4 parts per thousand, an order of magnitude smaller. This signal is larger than planetary signals that *WFIRST* will detect, but while the secondary eclipse presents itself as a sharp ingress and egress separated by a few hours, the phase curve signal is slowly varying over the course of the orbit. Its detection and characterization therefore requires any long-term systematics in the light curve to be well below the 400 part per million signal on few-day timescales.

If long-term systematics can indeed be maintained below the level of phase curve amplitudes in *WFIRST*, then we should expect to be able to observe a phase curve for many of the systems for which we observe a secondary eclipse, especially if they are tidally locked. We develop a simulated WASP-43 b phase curve around a 15th magnitude star by creating a sinusoidal signal with semiamplitude 200 parts per million and simulating observations, assuming the photometric uncertainty on each point is 1 part per thousand. We then model the phase curve signal by fitting two Fourier modes to the data corresponding to observations of the dayside of the planet, following the method of (Stevenson et al. 2014b). We fit the model and estimate the uncertainties on the fit, leading to an uncertainty on the time of the brightest point, using the *emcee* package (Goodman & Weare 2010; Foreman-Mackey et al. 2013). From this fit, we measure an uncertainty of 3.7 degrees in our calculation of the time of maximum, or 11 degrees at $3\sigma$. Formally, this would lead to a $3\sigma$ detection of a 12 degree offset similar to the observed offset for WASP-43 b, but detailed characterization of the planet's atmosphere would be limited.

Given our selection of planet, host star magnitude, and neglect of systematics, this represents a best-case scenario: the best cases could produce marginal detections of an offset at the $3\sigma$ level, but more detailed characterization will not be possible. Therefore, it is likely that at best *WFIRST* phase curves will represent a chance to probe day-night temperature contrasts of hot Jupiters with observed secondary eclipses, but the prospects for a better understanding of these phase curves, such as detailed atmospheric transport, appears bleak.

#### 5.3.2. *Reflected Light*

In addition to thermal emission, there is also an observable signal in reflected light from the host star, which often dominates the phase curve signal in *Kepler* data (Shporer & Hu 2015). For *WFIRST* we do not expect this signal to be significant. The reflected light signal has amplitude

$$\frac{F_R}{F_0} = A_\lambda \left( \frac{2a}{R_p} \right)^2, \tag{2}$$

where $F_R$ is the amplitude of the signal, $F_0$ the flux from the star, $A_\lambda$ the albedo, $a$ the orbital semimajor axis and $R_p$ the planet radius.

While albedos are $\sim 0.1$ in the optical, averaged across W149 the albedo for giant planets is typically $\sim 10^{-3}$. For the orbital parameters of WASP-43 b, we would then expect the amplitude of the signal to be $\sim 10^{-7}$, well below what is observable. Typical albedos in the Z087 bandpass will be on the order of $10^{-2}$, so the amplitude of the signal will be an order of magnitude larger, but as the number of observations in this bandpass will be a factor of 50 lower, negating much of this benefit and making systematics harder to identify and mitigate.

#### 5.3.3. *Doppler Beaming*

As a planet and host star orbit their mutual center of mass, the flux emitted from the star is beamed towards the direction of travel due to the changing the velocity of the host star. A consequence of special relativity, the signal is observable at the non-relativistic speeds at which stars move during their orbits. To first order, the amplitude of the beaming signal is

$$\frac{F_D}{F_0} = (3 - \alpha) \frac{K_s}{c} \tag{3}$$

where $F_D$ is the amplitude of the signal, $F_0$ the flux from the stationary star, $\alpha$ the shape of the SED at the ob-

served wavelength, $K_s$ the Doppler semiamplitude of the star, and $c$ the speed of light (Loeb & Gaudi 2003). The SED is relevant because, as the star's velocity is modulated, the Doppler shift affects what features of the stellar spectrum fall in our bandpass. For most stars, the W149 filter will fall on the Rayleigh-Jeans tail of the SED, where $\alpha = 2$.

For a typical hot Jupiter ($K_s \sim 150$ m s$^{-1}$), the beaming amplitude will be $\sim 0.5$ parts per million, well below the sensitivity of *WFIRST*. However, this effect will be useful for detecting more massive objects of similar radii masquerading as hot Jupiters, such as brown dwarfs or very low mass stars. A 50 $M_{Jup}$ object with a three-day period would exhibit a 25-ppm signal. In Section 3.1 we determined that we can measure a transit depth to a precision of 40 ppm. That transit event has a duration of 1.5 hours, whereas the beaming signal occurs throughout the orbit. This implies that beaming will be measured in many of these false positive scenarios. However, the smooth, sinusoidal signature of the beaming signals may be harder to distinguish from instrumental noise than the sharp box-shaped signature of a transit. Moreover, if the secondary is luminous in the *WFIRST* bandpass, it will exhibit its own Doppler beaming signal which will destructively interfere with the primary signal, reducing the magnitude of the observable effect (Shporer et al. 2010).

#### 5.3.4. *Ellipsoidal Variations*

Ellipsoidal variations are an achromatic phenomenon caused by changes in the sky-projected shape of a star as a planet orbits, affecting the star's gravitational potential. The signal has twice the frequency of the planet's orbit. Following Loeb & Gaudi (2003), to first order the magnitude of the signal is

$$\frac{F_E}{F_0} \sim \beta \frac{M_p}{M_s} \left( \frac{a}{R_s} \right)^{-3}, \quad (4)$$

Here, $\beta$ is a term which depends on the nature of gravity darkening for the host star. For Sun-like stars, this value is approximately 0.45. $M_p/M_s$ is the mass ratio between the planet and star and $a/R_s$ is the reduced orbital semimajor axis.

In general, the signal is of a similar magnitude to the Doppler beaming signal, and only likely to be useful in separating brown dwarfs from planets: transiting planets will only be notable by a nondetection of their ellipsoidal variations.

McDonald et al. (2014) note that in the case of *Euclid*, a color-dependence in observed ellipsoidal variations would be a signature of a background eclipsing binary, as the signal would be achromatic but the relative flux between the foreground and background target would vary between the two bandpasses. The same is true here, although with the cadence of Z087 observations we do not expect this effect to be detectable. In any cases where such an effect would be detectable, variations in the eclipse depth between the bandpasses would also be detectable, likely at a much higher significance. Unlike the Doppler beaming case, because the signal occurs at twice the orbital period, additional signals from a luminous secondary would constructively interfere with the signal from the primary, making the signal even easier to detect.

### 5.4. *Ground-based followup*

Ground-based adaptive optics imaging is typically used to rule out false positive blends of nearby star systems and to understand the level of dilution in transit light curves (Law et al. 2014). In principle, the transiting planet candidates discovered by *WFIRST* can be followed up by adaptive optics (AO) systems on 10-meter telescopes, or upcoming 30-meter class telescopes that are expected to be built before the *WFIRST* launch date. These observations may not provide much leverage over the *WFIRST* data themselves. The diffraction limit of a 30-meter telescope in $K$-band is $\sim 20$ milliarcseconds. While considerably smaller than the *WFIRST* pixel scale of $0\farcs11$/pixel, this still corresponds to a projected separation of $\approx$20 au for a Sun-like star with W149 = 14.5, at a distance of $\approx$1 kpc. The diffraction limit also corresponds to a projected separation of 200 au for a Sun-like star at 1 kpc with W149 = 19.5, meaning many bound binary companions will be unresolved even when operating a thirty-meter telescope at the diffraction limit.

## 6. GALACTIC EXOPLANET DEMOGRAPHICS

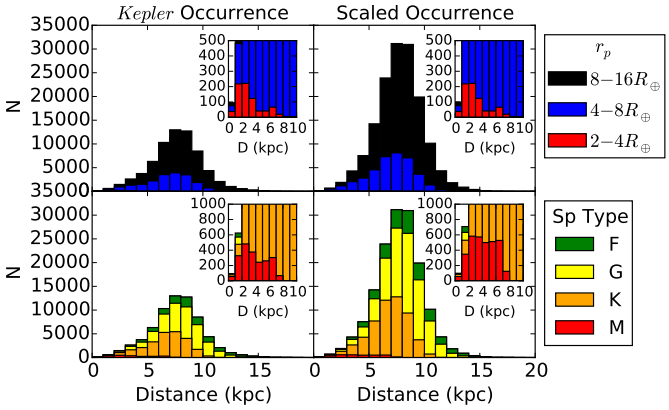


FIG. 8.— The distribution of simulated transiting planets as a function of galactic distance. The left panels assume the planet occurrence rate is identical to that of *Kepler*; the right panels assume the occurrence rate scales with metallicity. The top panels show the breakdown of planet discoveries as a function of planet radius, and the bottom panels show the breakdown as a function of host spectral type. The insets highlight the distributions for small planets (top) and small stars (bottom) for which the total numbers are comparatively small.

With the simulation described in Section 3.2, we are also able to evaluate the number of transiting planets that will be discovered by *WFIRST* as a function of distance from the Sun. Gould et al. (2015) contains a detailed discussion of measuring parallaxes with *WFIRST*, including a discussion of the potential sources of systematic errors. In summary, *WFIRST* will have a single measurement, astrometric precision of 0.7 mas for stars as faint as $H_{AB} = 19.6$ and 1.7 mas for $H_{AB} = 21.6$ (Spergel et al. 2015). Given that there will be 40,000 measurements of each star over the course of the mission, in the absence of severe systematics, Gould et al.

(2015) determine *WFIRST* should measure the relative parallaxes of all planets considered in this study. These relative parallaxes can also be tied to the *Gaia* system to determine the absolute parallaxes.

In real data, determining the distances to stars may be more difficult. We will not understand each pixel perfectly, so there should be underlying systematic effects. A reasonable comparison case may be the astrometry achieved by using the spatial scan mode of *HST* (Riess et al. 2014). This method leads to an astrometric precision of 20-40 $\mu$as. The pixels of *WFIRST* are a factor of two larger, which would lead to a factor of two larger uncertainty on the parallax. If the systematics can be controlled to this level (i.e. 80 $\mu$as), then *WFIRST* can measure $3\sigma$ parallaxes out to 4 kpc and place upper limits beyond that. It should then be possible to construct a sample of known disk stars with measured parallaxes and a sample of probable bulge stars with parallaxes consistent with zero.

Even with no distance measurements, it will still be possible to investigate the Galactic distribution of hot and warm planets. The different Galactic stellar populations have different proper motion distributions. WFIRST's astrometric precision will be easily good enough to measure accurate proper motions for each planet host, and with a large population of planet hosts it will be possible to select large, statistically clean samples of bulge and disk planets in the same way that is currently done for stars (Clarkson et al. 2008).

Figure 6 shows the distribution of planets from our simulation as a function of distance from the Sun. These planets are distributed all along the line of sight, including into the bulge of the galaxy. Of particular interest are planets that can be directly confirmed via secondary eclipses. Their distribution is shown in Figure 7. Given that *WFIRST* should detect thousands of confirmed hot Jupiters, it will be possible to study their distribution towards the center of the galaxy. This measurement will test the variation in occurrence rate of short-period giant planets in the disk and the bulge, and whether or not planet formation is suppressed in the bulge as suggested by Thompson (2013).

## 7. CONCLUSIONS

While ostensibly a microlensing mission, *WFIRST* will provide a tremendous opportunity for the study of short-period, transiting planets as well. We have shown in Section 3.2 that if the occurrence rate of planets is the same as for the main *Kepler* field, *WFIRST* could detect 70,000 transiting planets with sizes as small as $2R_\oplus$ at distances of up to 10 kpc or more. If the occurrence rate scales with metallicity as in Johnson et al. (2010), we expect as many as 150,000 planets, as the *WFIRST* field is more metal-rich than the solar neighborhood. All of these systems should have measured parallaxes (Gould et al. 2015).

While the vast majority of these planets will be found around stars too faint for followup observations, we explore various options for confirming or validating these planets directly from the *WFIRST* data. We find that secondary eclipse depth measurements can be used to confirm as many as 2,900 giant planets, which can be detected at distances of $> 8$ kpc. From these confirmed *WFIRST* planets, we will be able to measure the variation in the occurrence rate of short-period giant planets. Furthermore, we show that *WFIRST* is capable of detecting transit timing variations which can be used to confirm the planetary nature of some systems, especially those with smaller planets.

The transiting planets found by *WFIRST*, especially those that can be confirmed, will provide unprecedented information about how planetary system architectures vary with galactic environment. Although the transiting planets and *WFIRST* microlensing planets will generally not be found around the same host stars, both samples probe the same planetary population but at very different planetary separations. Figures 14 and 15 of McDonald et al. (2014) summarize the complementarity of the two techniques in the context of *Euclid*. It is clear that by combining the two samples of planets, we can probe planetary system architecture from very small separations to beyond 10 au.

We thank Avi Shporer (JPL) for comments which improved the quality of this manuscript.

Work by B.T.M., J.C.Y., and M.T.P. was performed in whole or in part under contract with the California Institute of Technology (Caltech)/Jet Propulsion Laboratory (JPL) funded by NASA through the Sagan Fellowship Program executed by the NASA Exoplanet Science Institute. This research has made use of the NASA Exoplanet Archive, which is operated by the California Institute of Technology, under contract with the National Aeronautics and Space Administration under the Exoplanet Exploration Program.

## REFERENCES

Agol, E., Steffen, J., Sari, R., & Clarkson, W. 2005, MNRAS, 359, 567
Ammons, S. M., Robinson, S. E., Strader, J., et al. 2006, ApJ, 638, 1004
Angerhausen, D., DeLarme, E., & Morse, J. A. 2015, PASP, 127, 1113
Ballard, S., Fabrycky, D., Fressin, F., et al. 2011, ApJ, 743, 200
Baraffe, I., Homeier, D., Allard, F., & Chabrier, G. 2015, A&A, 577, A42
Barclay, T., Quintana, E. V., Adams, F. C., et al. 2015, ApJ, 809, 7
Batista, V., Beaulieu, J.-P., Gould, A., et al. 2014, ApJ, 780, 54
Becker, J. C., Vanderburg, A., Adams, F. C., Rappaport, S. A., & Schwengeler, H. M. 2015, ApJ, 812, L18
Bennett, D. P., & Rhie, S. H. 2002, ApJ, 574, 985
Bilir, S., Ak, S., Karaali, S., et al. 2008, MNRAS, 384, 1178
Borucki, W. J., Koch, D., Basri, G., et al. 2010, Science, 327, 977
Bouchy, F., Pont, F., Melo, C., et al. 2005, A&A, 431, 1105
Buchhave, L. A., & Latham, D. W. 2015, ApJ, 808, 187
Calamida, A., Sahu, K. C., Casertano, S., et al. 2015, ApJ, 810, 8
Calchi Novati, S., Gould, A., Udalski, A., et al. 2015, ApJ, 804, 20
Campante, T. L., Handberg, R., Mathur, S., et al. 2011, A&A, 534, A6
Cardelli, J. A., Clayton, G. C., & Mathis, J. S. 1989, ApJ, 345, 245
Chabrier, G., & Baraffe, I. 1997, A&A, 327, 1039
Charbonneau, D., Allen, L. E., Megeath, S. T., et al. 2005, ApJ, 626, 523
Christiansen, J. L., Jenkins, J. M., Caldwell, D. A., et al. 2012, PASP, 124, 1279

Cirasuolo, M., Afonso, J., Bender, R., et al. 2012, in Proc. SPIE, Vol. 8446, Ground-based and Airborne Instrumentation for Astronomy IV, 84460S
Claret, A., & Bloemen, S. 2011, A&A, 529, A75
Clarkson, W., Sahu, K., Anderson, J., et al. 2008, ApJ, 684, 1110
Croll, B., Lafreniere, D., Albert, L., et al. 2011, AJ, 141, 30
Crossfield, I. J. M., Ciardi, D. R., Petigura, E. A., et al. 2016, ApJS, 226, 7
Cumming, A., Butler, R. P., Marcy, G. W., et al. 2008, PASP, 120, 531
Dawson, R. I., & Murray-Clay, R. A. 2013, ApJ, 767, L24
Deck, K. M., Agol, E., Holman, M. J., & Nesvorný, D. 2014, ApJ, 787, 132
Dreizler, S., Hauschildt, P. H., Kley, W., et al. 2003, A&A, 402, 791
Eastman, J., Gaudi, B. S., & Agol, E. 2013, PASP, 125, 83
Esteves, L. J., De Mooij, E. J. W., & Jayawardhana, R. 2013, ApJ, 772, 51
Fabrycky, D. C., Ford, E. B., Steffen, J. H., et al. 2012, ApJ, 750, 114
Faigler, S., Kull, I., Mazeh, T., et al. 2015, ApJ, 815, 26
Faigler, S., & Mazeh, T. 2011, MNRAS, 415, 3921
—. 2015, ApJ, 800, 73
Fischer, D. A., & Valenti, J. 2005, ApJ, 622, 1102
Ford, E. B. 2014, Proceedings of the National Academy of Science, 111, 12616
Ford, E. B., Fabrycky, D. C., Steffen, J. H., et al. 2012, ApJ, 750, 113
Foreman-Mackey, D., Hogg, D. W., Lang, D., & Goodman, J. 2013, PASP, 125, 306
Foreman-Mackey, D., Montet, B. T., Hogg, D. W., et al. 2015, ApJ, 806, 215
Foreman-Mackey, D., Morton, T. D., Hogg, D. W., Agol, E., & Schölkopf, B. 2016, AJ, 152, 206
Gilliland, R. L., Brown, T. M., Christensen-Dalsgaard, J., et al. 2010, PASP, 122, 131
Goodman, J., & Weare, J. 2010, Communications in Applied Mathematics and Computational Science, 5, 65
Gould, A., Huber, D., Penny, M., & Stello, D. 2015, Journal of Korean Astronomical Society, 48, 93
Haas, M. R., Batalha, N. M., Bryson, S. T., et al. 2010, ApJ, 713, L115
Hadden, S., & Lithwick, Y. 2014, ApJ, 787, 80
Hellier, C., Anderson, D. R., Collier Cameron, A., et al. 2011, A&A, 535, L7
Holczer, T., Shporer, A., Mazeh, T., et al. 2015, ApJ, 807, 170
Holczer, T., Mazeh, T., Nachmani, G., et al. 2016, ApJS, 225, 9
Holman, M. J., & Murray, N. W. 2005, Science, 307, 1288
Holman, M. J., Fabrycky, D. C., Ragozzine, D., et al. 2010, Science, 330, 51
Howard, A. W., Marcy, G. W., Bryson, S. T., et al. 2012, ApJS, 201, 15
Johnson, J. A., Aller, K. M., Howard, A. W., & Crepp, J. R. 2010, PASP, 122, 905
Johnson, J. A., Clanton, C., Howard, A. W., et al. 2011, ApJS, 197, 26
Jontof-Hutter, D., Rowe, J. F., Lissauer, J. J., Fabrycky, D. C., & Ford, E. B. 2015, Nature, 522, 321
Jontof-Hutter, D., Ford, E. B., Rowe, J. F., et al. 2016, ApJ, 820, 39
Kipping, D. M. 2010, MNRAS, 409, L119
Knutson, H. A., Charbonneau, D., Allen, L. E., et al. 2007, Nature, 447, 183
Knutson, H. A., Charbonneau, D., Cowan, N. B., et al. 2009, ApJ, 690, 822
Konacki, M., Torres, G., Sasselov, D. D., & Jha, S. 2003, ApJ, 597, 1076
Kroupa, P. 2001, MNRAS, 322, 231
Law, N. M., Morton, T., Baranec, C., et al. 2014, ApJ, 791, 35
Lillo-Box, J., Barrado, D., Moya, A., et al. 2014, A&A, 562, A109
Lissauer, J. J., Ragozzine, D., Fabrycky, D. C., et al. 2011, ApJS, 197, 8
Lissauer, J. J., Marcy, G. W., Rowe, J. F., et al. 2012, ApJ, 750, 112
Lithwick, Y., & Wu, Y. 2012, ApJ, 756, L11
Loeb, A., & Gaudi, B. S. 2003, ApJ, 588, L117
Maciejewski, G., Dimitrov, D., Fernández, M., et al. 2016, A&A, 588, L6
Mandel, K., & Agol, E. 2002, ApJ, 580, L171
Mayor, M., Marmier, M., Lovis, C., et al. 2011, ArXiv e-prints, arXiv:1109.2497
Mazeh, T., Nachmani, G., Holczer, T., et al. 2013, ApJS, 208, 16
McDonald, I., Kerins, E., Penny, M., et al. 2014, MNRAS, 445, 4137
Mislis, D., Heller, R., Schmitt, J. H. M. M., & Hodgkin, S. 2012, A&A, 538, A4
Montet, B. T., Crepp, J. R., Johnson, J. A., Howard, A. W., & Marcy, G. W. 2014, ApJ, 781, 28
Montet, B. T., Morton, T. D., Foreman-Mackey, D., et al. 2015, ApJ, 809, 25
Morton, T. D. 2012, ApJ, 761, 6
—. 2015, VESPA: False positive probabilities calculator, Astrophysics Source Code Library, ascl:1503.011
Morton, T. D., Bryson, S. T., Coughlin, J. L., et al. 2016, ApJ, 822, 86
Morton, T. D., & Johnson, J. A. 2011, ApJ, 738, 170
Morton, T. D., & Swift, J. 2014, ApJ, 791, 10
Nataf, D. M., Gould, A., Fouqué, P., et al. 2013, ApJ, 769, 88
Nesvorný, D., Kipping, D., Terrell, D., et al. 2013, ApJ, 777, 3
Nesvorný, D., Kipping, D. M., Buchhave, L. A., et al. 2012, Science, 336, 1133
Osborn, H. P., Armstrong, D. J., Brown, D. J. A., et al. 2016, MNRAS, 457, 2273
Otor, O. J., Montet, B. T., Johnson, J. A., et al. 2016, AJ, 152, 165
Pedicelli, S., Bono, G., Lemasle, B., et al. 2009, A&A, 504, 81
Penny, M. T., Henderson, C. B., & Clanton, C. 2016a, ApJ, 830, 150
Penny, M. T., Rattenbury, N. J., Gaudi, B. S., & Kerins, E. 2016b, ArXiv e-prints, arXiv:1605.01059
Quinn, S. N., White, T. R., Latham, D. W., et al. 2015, ApJ, 803, 49
Quintana, E. V., Rowe, J. F., Barclay, T., et al. 2013, ApJ, 767, 137
Ragozzine, D., & Wolf, A. S. 2009, ApJ, 698, 1778
Riess, A. G., Casertano, S., Anderson, J., MacKenty, J., & Filippenko, A. V. 2014, ApJ, 785, 161
Robin, A. C., Reylé, C., Derrière, S., & Picaud, S. 2003, A&A, 409, 523
Rolleston, W. R. J., Smartt, S. J., Dufton, P. L., & Ryans, R. S. I. 2000, A&A, 363, 537
Sahu, K. C., Casertano, S., Bond, H. E., et al. 2006, Nature, 443, 534
Salpeter, E. E. 1955, ApJ, 121, 161
Schlaufman, K. C., & Winn, J. N. 2013, ApJ, 772, 143
Shporer, A., & Hu, R. 2015, AJ, 150, 112
Shporer, A., Kaplan, D. L., Steinfadt, J. D. R., et al. 2010, ApJ, 725, L200
Shporer, A., Jenkins, J. M., Rowe, J. F., et al. 2011, AJ, 142, 195
Spergel, D., Gehrels, N., Baltay, C., et al. 2015, ArXiv e-prints, arXiv:1503.03757
Steffen, J. H., Ragozzine, D., Fabrycky, D. C., et al. 2012, Proceedings of the National Academy of Science, 109, 7982
Stevenson, K. B., Bean, J. L., Madhusudhan, N., & Harrington, J. 2014a, ApJ, 791, 36
Stevenson, K. B., Désert, J.-M., Line, M. R., et al. 2014b, Science, 346, 838
Stevenson, K. B., Line, M. R., Bean, J. L., et al. 2016, ArXiv e-prints, arXiv:1608.00056
Thompson, T. A. 2013, MNRAS, 431, 63
Udalski, A., Zebrun, K., Szymanski, M., et al. 2002a, Acta Astronomica, 52, 115
Udalski, A., Paczynski, B., Zebrun, K., et al. 2002b, Acta Astronomica, 52, 1
Udry, S., Bonfils, X., Delfosse, X., et al. 2007, A&A, 469, L43
Uehara, S., Kawahara, H., Masuda, K., Yamada, S., & Aizawa, M. 2016, ApJ, 822, 2
Valenti, J. A., & Fischer, D. A. 2005, ApJS, 159, 141
Vanderburg, A., Latham, D. W., Buchhave, L. A., et al. 2016, ApJS, 222, 14
Wang, J., Fischer, D. A., Horch, E. P., & Huang, X. 2015a, ApJ, 799, 229

Wang, J., Xie, J.-W., Barclay, T., & Fischer, D. A. 2014, ApJ, 783, 4
Wang, J., Fischer, D. A., Barclay, T., et al. 2015b, ApJ, 815, 127
Wright, J. T., Marcy, G. W., Howard, A. W., et al. 2012, ApJ, 753, 160
Xie, J.-W. 2013, ApJS, 208, 22
Yee, J. C., & Gaudi, B. S. 2008, ApJ, 688, 616